Nano Research

Open Access

Research Article

Superelastic isotropic carbon aerogel with spherical cavity structure

Wei Qian[1], Huazhang Zhang[1], Lun Li[1], Pengfei Chen[2], Xun Li[2], Peng Li[1], Zhe Wang[3] ✉, and Daping He[1] ✉

[1] *Hubei Engineering Research Center of Radio Frequency Microwave Technology and Application, School of Physics and Mechanics, Wuhan University of Technology, Wuhan 430070, China*
[2] *School of Materials Science and Engineering, Wuhan University of Technology, Wuhan 430070, China*
[3] *State Key Laboratory of Advanced Technology for Materials Synthesis and Processing, Wuhan University of Technology, Wuhan 430070, China*

Cite this article: *Nano Research*, **2025**, *18*, 94907690. https://doi.org/10.26599/NR.2025.94907690

ABSTRACT: To address the issue of mechanical heterogeneity and structural failure in traditional anisotropic aerogels under complex stress fields, this study proposes a synergistic strategy combining bubble templating with freeze-casting. This approach enables the fabrication of an elastic carbon aerogel with three-dimensionally isotropic structural characteristics. Using aramid nanofibers as the matrix skeleton, the incorporation of graphene oxide reduces the surface tension of the solution while enhancing system viscosity, effectively suppressing bubble coalescence and ultimately yielding a carbon aerogel with a spherical cavity structure. The resulting aerogel exhibits nearly identical physical properties across all three spatial dimensions. Notably, it maintains exceptional structural stability (plastic deformation < 2.9%) even under 80% compressive strain and demonstrates ultra-wide temperature adaptability. This work provides a novel design strategy for high-performance porous materials.

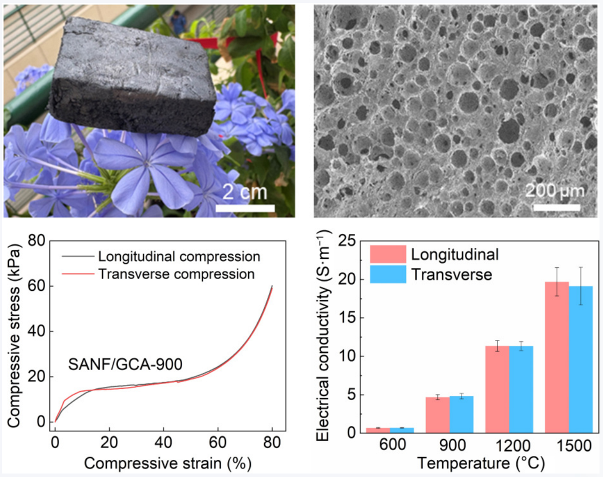

KEYWORDS: isotropic, carbon aerogels, spherical cavity structures, bubble-templating

1 Introduction

Porous materials have demonstrated revolutionary application prospects in aerospace engineering [1], energy storage systems [2, 3], and advanced thermal management solutions [4–6], owing to their unique characteristics of lightweight nature [7, 8], high specific surface area [9], and tunable physicochemical properties [10]. As a representative paradigm of this material system, carbon aerogels have successfully expanded their application potential in extreme service conditions through the sophisticated integration of the exceptional electrical conductivity [10, 11], superior chemical stability [12, 13], and characteristic ultralow density of carbon-based materials coupled with three-dimensional (3D) interconnected porous networks inherent to aerogels [14–16]. This remarkable combination has established them as highly competitive candidate materials for cutting-edge technological domains, including next-generation thermal protection systems [17], flexible electronics [10], and intelligent sensing modules [18]. Notably, the intrinsic mechanical heterogeneity exhibited by conventional anisotropic carbon aerogels under complex stress fields frequently induces microstructural instability and macroscopic performance degradation [15, 19]. This inherent limitation has significantly constrained their practical implementation in high-reliability engineering applications. Consequently, the development of carbon aerogels featuring 3D isotropic architectures and elastic recovery characteristics has emerged as a pivotal research direction to overcome current engineering application bottlenecks. Such advancements hold substantial significance for achieving long-term structural integrity and functional reliability under multi-physical field coupling conditions, which are particularly critical for maintaining material performance in sophisticated operational environments.

In conventional carbon aerogel fabrication, although directional freezing can achieve mechanical reinforcement along specific orientations by constructing unidirectional lamellar pore

---

Received: May 25, 2025; **Revised:** June 9, 2025
Accepted: June 12, 2025

✉Address correspondence to Zhe Wang, wangzhe0614@whut.edu.cn; Daping He, hedaping@whut.edu.cn

channels [20–22], it inevitably introduces significant 3D performance anisotropy. When subjected to multiaxial loading or dynamic stresses, anisotropic structures tend to induce stress concentration, ultimately resulting in catastrophic structural failure. To address this challenge, researchers have explored various porous material construction strategies through biomimetic structural design. The bubble-templating method has attracted considerable attention due to its precise control over pore morphology [23], yet conventional foaming techniques are limited by bubble coalescence and Ostwald ripening effects, making it difficult to obtain uniform and stable 3D hierarchical pore structures. Meanwhile, freeze-casting techniques can guide material assembly via ice crystal growth, but the unidirectional structures formed during single freezing processes struggle to overcome anisotropy limitations [24, 25]. Achieving synergistic control over material assembly behavior across molecular, mesoscopic, and macroscopic scales to construct carbon aerogels with 3D mechanical homogeneity and thermal stability remains an urgent challenge in this field.

This study innovatively proposes a synergistic assembly strategy combining bubble templating with freeze-casting, successfully fabricating elastic carbon aerogels with 3D isotropic characteristics. Using aramid nanofiber (ANF) as the structural frameworks and introducing graphene oxide (GO) as an interfacial regulator to reduce solid–liquid interfacial tension and enhance system viscosity, bubble coalescence was effectively suppressed, which improved kinetic stability of the foaming system. This multicomponent synergy effect enables the formation of uniformly distributed spherical ANF/GO aerogels (SANF/GOA) during the freeze-forming process. After carbonization, spherical ANF/graphene carbon aerogels (SANF/GCA) exhibited plastic deformation of less than 2.9% at 80% compressive strain and demonstrated exceptional adaptability across a wide temperature range (−196 to 500 °C). Thermal analysis revealed a thermal conductivity below 84.2 $\mathrm{mW \cdot m^{-1} \cdot K^{-1}}$ and an anisotropy index smaller than 1.06. This work provides a novel methodology for designing high-performance porous materials with significant application prospects in extreme-environment thermal management and related fields.

2 Results and discussion

2.1 Structural design and fabrication of SANF/GCA

The fabrication process of SANF/GCA is schematically depicted in Fig. 1(a). Initially, ANF aqueous dispersion was prepared via a proton donor-assisted deprotonation method (Fig. S1 in the Electronic Supplementary Material (ESM)) [25], and GO was obtained via mechanical exfoliation (Fig. S2 in the ESM). Under mechanical stirring, GO was uniformly dispersed into ANF matrix, forming a stable and homogeneous composite suspension system. Subsequently, a foaming process was carried out: Sodium dodecyl sulfate (SDS) was introduced as a surfactant, promoting rapid bubble nucleation and generating a 3D network of uniformly distributed microbubbles through vigorous gas–liquid interfacial interactions (Fig. S3 in the ESM). The resulting foam-structured suspension was transferred into a custom mold and instantaneously cryo-fixed by immersion in liquid nitrogen, effectively preserving the hierarchical bubble architecture. Subsequent lyophilization under vacuum removed the frozen solvent, yielding a mechanically robust SANF/GOA with a well-defined porous morphology. Finally, thermal annealing at elevated temperatures simultaneously carbonizes the organic components, producing an isotropic elastic carbon aerogel with enhanced structural integrity and compressibility.

Compared to conventional directional freezing methods for carbon aerogel fabrication [22, 26, 27], our approach integrates rapid bubble templating with the scalability of freeze-casting, enabling efficient, controllable, and reproducible preparation of SANF/GCA. As demonstrated in Fig. 1(b), a 12 $\mathrm{cm^3}$ SANF/GCA monolith delicately balances on a flower petal, underscoring its

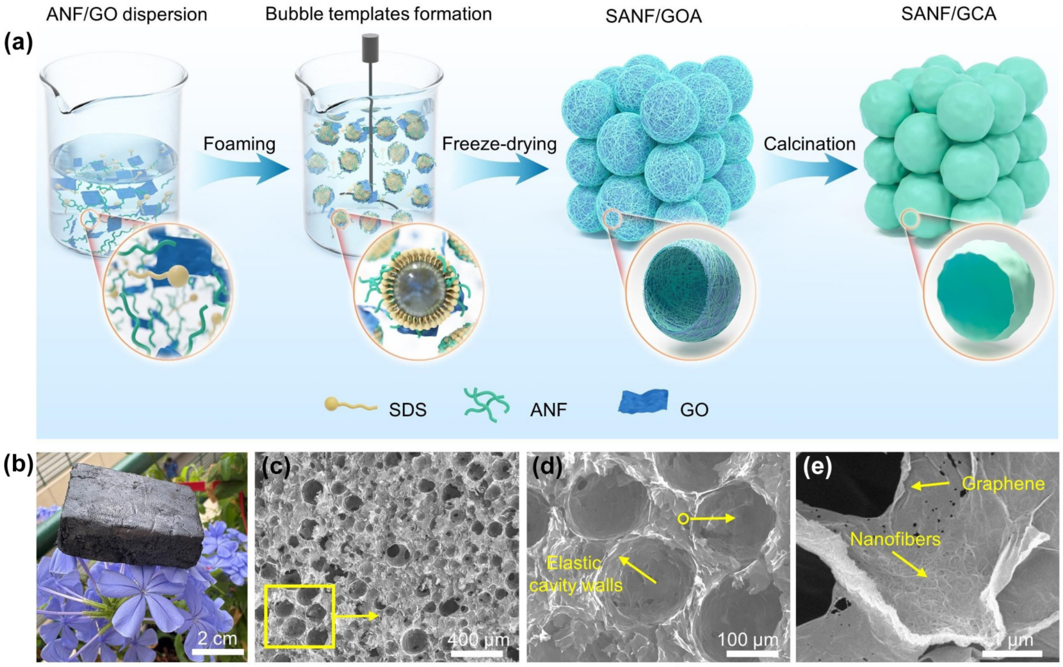

Figure 1 Synthesis process and structural characterization of SANF/GCA. (a) Schematic diagram illustrating the stepwise fabrication process of SANF/GCA. (b) Optical image of SANF/GCA. (c)–(e) SEM images of SANF/GCA at different magnifications.

ultralight nature. Under the structural guidance of gas bubble templates, nanofibers and nanosheets co-assemble into isotropic spherical cavities within the 3D framework. Scanning electron microscopy (SEM) images (Figs. 1(c)–1(e)) reveal a hierarchical architecture comprising cascaded spherical pores, discrete cellular compartments, and mechanically reinforced interlocking nodes. Due to mutual electrostatic repulsion resulting from their high electronegativity, GO forms a continuous skeletal network, while ANF uniformly anchors across this framework, ensuring homogeneous integration (Fig. S4 in the ESM). During rapid freezing of the microbubble-laden dispersion, spatial confinement between adjacent microbubbles guides the precise alignment of constituents along interfacial boundaries. Simultaneously, synergistic space-partitioning effects from microbubbles and growing ice crystals promote progressive accumulation of components along bubble peripheries. Post freeze-drying and thermal treatment preserve this configuration, yielding a mechanically integrated, hierarchically structured aerogel with cascaded spherical porosity.

2.2 Regulation of bubble stability

The fabrication of SANF/GCA hinges critically on maintaining long-term stability of bubbles within the dispersion system. As illustrated in Fig. 2(a), when employing solely ANF dispersion, the low viscosity of the system fails to provide sufficient viscous resistance to anchor bubbles, resulting in the inability to form aerogels with well-defined spherical cavity structures (Fig. 2(b)). This study reveals that the introduction of GO effectively resolves this challenge through dual synergistic mechanisms: Firstly, GO nanosheets form a dense adsorption layer at the gas–liquid interface via their amphiphilic properties, with their two-dimensional structure significantly retarding liquid film thinning [28]. Secondly, the abundant oxygen-containing functional groups on GO surfaces establish hydrogen bonding and electrostatic crosslinking networks with SDS and ANF [29], substantially enhancing the mechanical strength of the liquid film. This synergistic effect enables successful preservation of uniform 3D spherical cavity morphology in the aerogel (Figs. 2(c) and 2(d) and Fig. S5 in the ESM).

From the perspective of microbubble mechanical equilibrium, bubble stability is governed by the dynamic balance between buoyancy and viscous resistance (Fig. 2(e)) [18, 30]. Experimental results demonstrate that GO incorporation markedly increases system viscosity (Fig. 2(f)), effectively suppressing bubble sedimentation through enhanced viscous resistance. More importantly, GO nanosheets regulate interfacial energy to inhibit Ostwald ripening driven by Laplace pressure differences. This inhibition effectively blocks gas diffusion pathways from smaller to larger bubbles, thereby significantly improving the uniformity of pore size distribution in the aerogel [23]. These findings provide both theoretical foundations and technical pathways for designing high-performance porous materials.

This study systematically elucidates the influence of

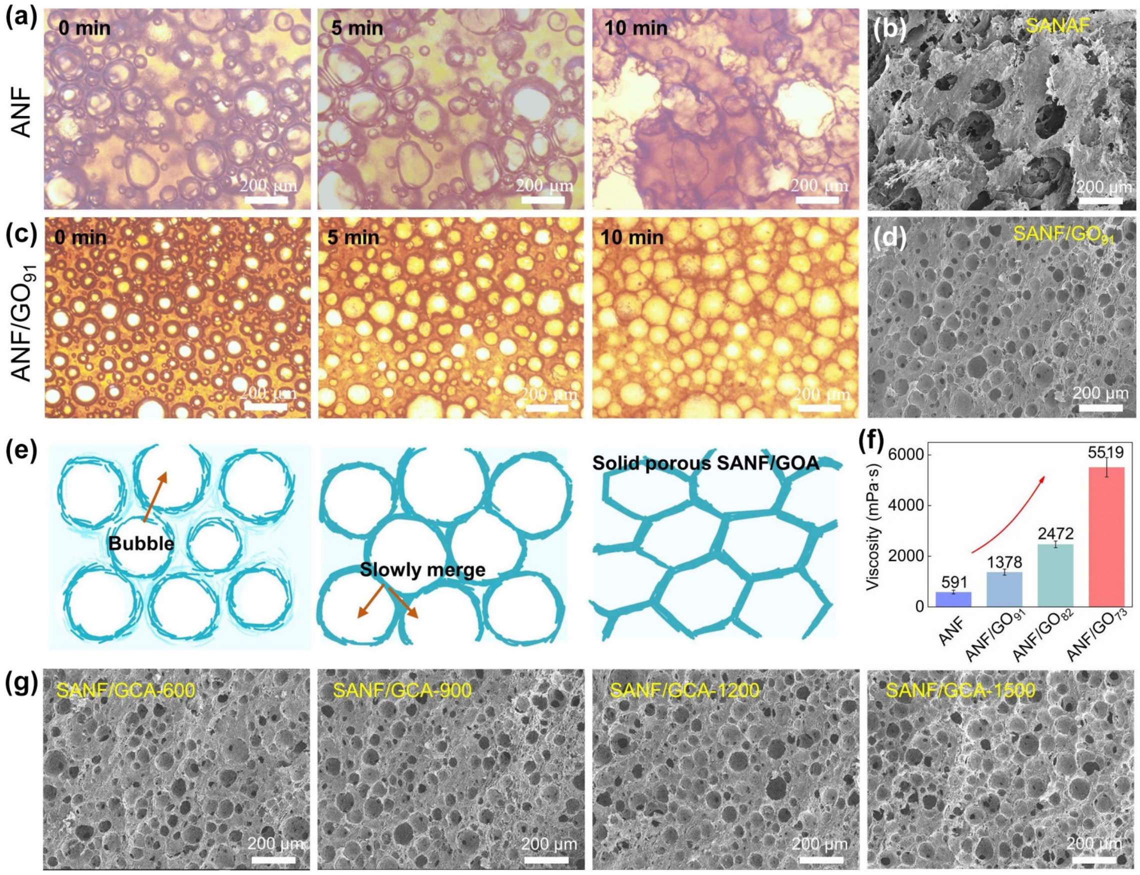

Figure 2 Regulation of bubble stability. (a) Optical microscopy sequences capturing *in situ* foaming dynamics of ANF during ambient drying. (b) SEM image of SANF. (c) Comparative optical microscopic sequences capturing *in situ* foaming dynamics of the ANF/GO$_{91}$ during ambient drying. (d) SEM image of SANF/GO$_{91}$. (e) Mechanistic diagram elucidating the structural evolution during hybrid aerogel formation. (f) The viscosity for ANF and ANF/GO composite slurries. (g) SEM images of SANF/GCA-600, SANF/GCA-900, SANF/GCA-1200, and SANF/GCA-1500.

carbonization temperature on the structural evolution and properties of SANF/GOA composite aerogels. As shown in Fig. 2(g), the spherical cavity structure of the aerogel exhibits remarkable thermal stability across a broad carbonization temperature range (600–1500 °C), retaining a uniform pore size distribution of 120 ± 12 μm, comparable to that of the pristine (non-carbonized) aerogel (Fig. S6 in the ESM). These findings suggest that pyrolysis minimally disrupts the 3D framework. Thermogravimetric analysis highlights distinct thermal behaviors between components: Below 450 °C, ANF undergo only an 11.2% mass loss due to bound water removal (Fig. S7 in the ESM), remaining in the pre-carbonization stage. In contrast, GO experiences significant mass loss (45.3%) within 200–450 °C, attributed to the release of interlayer water and the decomposition of oxygen-containing functional groups. This differential thermal degradation governs the density evolution. Upon carbonization at 600 °C, the aerogel density sharply decreases from 15.63 to 7.21 mg·cm^{-3} (Fig. S8 in the ESM). Beyond this threshold, density changes stabilize, reflecting the consolidation of the carbon skeleton and the near-exhaustion of volatile component release.

2.3 Thermally driven structural reconfiguration in SANF/GOA

Through systematic characterization techniques including Fourier transform infrared spectroscopy (FTIR), X-ray diffraction (XRD), Raman spectroscopy, and high-resolution transmission electron microscopy (HRTEM), the structural evolution of carbon aerogels during the preparation process was elucidated. As shown in Fig. 3(a), the FTIR spectrum of the SANF/GOA precursor underwent significant changes after carbonization: The characteristic absorption peaks corresponding to organic functional groups (O–H, C–O, N–H, and C–O–C) were nearly eliminated after high-temperature treatment at 600 °C. XRD analysis further verified the structural evolution (Fig. 3(b)). The initial SANF/GOA exhibited three characteristic diffraction peaks at 10.3°, 20.4°, and 23.1°, corresponding to the (001) crystal plane of graphene oxide and the (110) and (200) crystal planes of aramid nanofibers [31, 32], respectively, confirming the successful construction of the composite precursor. After carbonization, these precursor peaks completely disappeared, while a prominent diffraction peak emerged at approximately 24.5°, corresponding to the (002) crystal plane of graphite. Notably, as the carbonization temperature increased from 600 to 1500 °C, the full width at half maximum (FWHM) of the graphite peak gradually decreased, indicating that high-temperature treatment effectively promoted the growth and perfection of graphite microcrystals.

Raman spectroscopy provided crucial evidence for the evolution of carbon structural defects (Fig. 3(c)) [33]. All samples exhibited characteristic peaks at 1350 cm^{-1} (D band, disordered structure) and 1594 cm^{-1} (G band, graphitic structure). The intensity ratio (I_D/I_G) consistently decreased from 0.98 at 600 °C to 0.77 at 1500 °C, quantitatively demonstrating the enhancement of graphitization degree by high-temperature treatment, which corroborated the XRD results. When the temperature reached 1500 °C, the

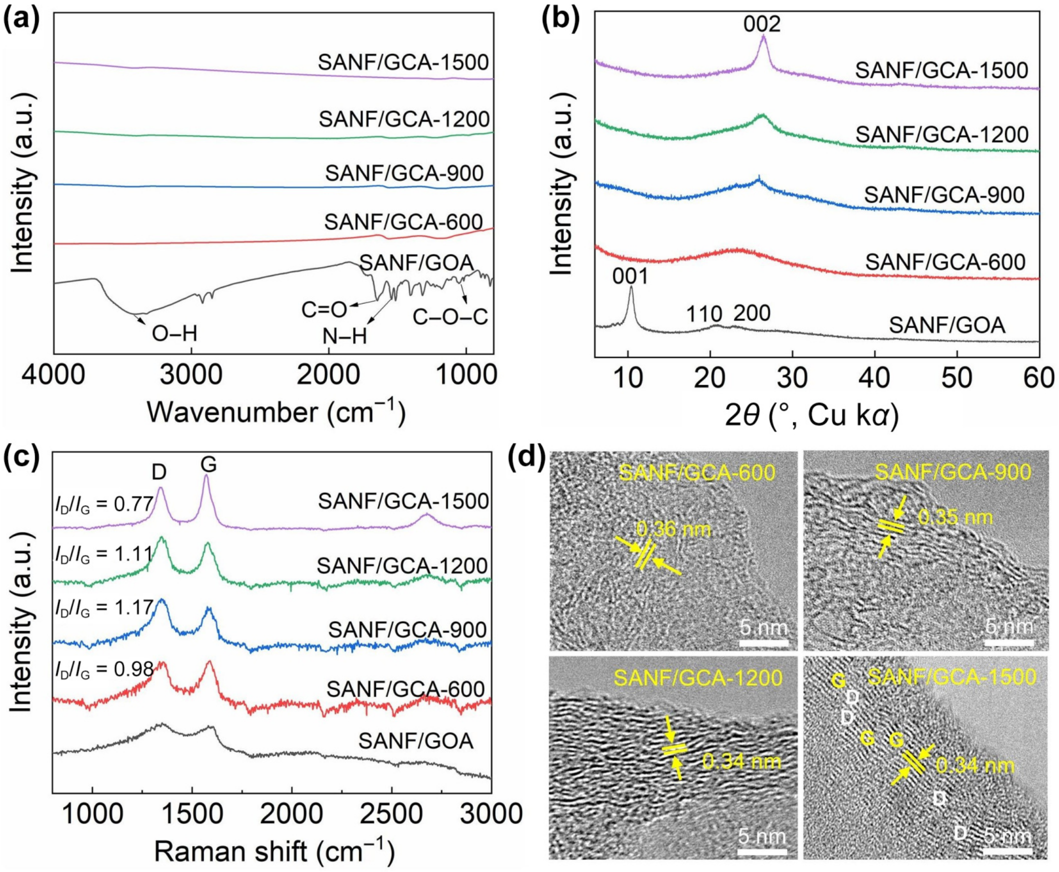

Figure 3 Thermally driven structural reconfiguration in SANF/GOA. (a) FTIR spectra revealing functional group transformations during pyrolysis. (b) XRD patterns analysis showing amorphous-to-crystalline transition. (c) Raman spectra deconvolution quantifying structural disorder through D-band to G-band intensity ratio evolution. (d) HRTEM images of SANF/GCA-600, SANF/GCA-900, SANF/GCA-1200, and SANF/GCA-1500.

appearance of a two-dimensional (2D) characteristic peak at 2695 cm^{-1} with a symmetric line shape indicated the formation of few-layer graphene domains with AB stacking structure within the material. The evolution of crystallinity and structural ordering in SANF/GOA during the heating process was further investigated by HRTEM (Fig. 3(d)). As the annealing temperature increased from 600 to 1500 °C, the elevated temperature environment facilitated the ordered rearrangement of the carbon skeleton and defect healing [34], as evidenced by a pronounced contraction of the interlayer lattice spacing from 0.36 to 0.34 nm, accompanied by a continuous enlargement of crystallite size. These structural evolution characteristics were well corroborated by XRD-derived crystal parameters and Raman-based defect concentration analysis, collectively elucidating the lattice perfection mechanism during high-temperature annealing.

2.4 Mechanical performance of SANF/GCA

The macroscopic properties of aerogels are intrinsically governed by their microstructures, particularly manifested in mechanical responses and thermal conduction characteristics. Unlike conventional aerogels with pronounced anisotropy, SANF/GCA exhibits remarkable isotropy owing to its unique three-dimensional spherical cavity interpenetrating architecture. Comparative quasi-static compression tests at 80% strain along transverse and longitudinal directions revealed nearly identical stress–strain curves in both principal orientations (Figs. 4(a) and 4(b)), confirming the isotropic nature of SANF/GCA. The characteristic compression curve demonstrates a triphasic evolution: (i) initial linear elastic region, (ii) intermediate plateau stage, and (iii) final abrupt stress escalation zone. These distinct regimes correspond to three deformation mechanisms: elastic bending of pore walls, subsequent elastic buckling, and eventual densification. Cyclic loading–unloading tests indicated negligible residual deformation (< 20% strain) and maintained structural integrity after 80% compression (Fig. 4(c) and Fig. S9 in the ESM).

The anti-fatigue performance test results demonstrated that during cyclic loading tests, SANF/GCA-900 exhibited exceptional deformation recovery capability after 1000 cycles at 60% strain (Fig. 4(d)). Specifically, it maintained a height retention rate of 92.2%, with a 34.5% reduction in ultimate stress (decreasing from 22.9 to 15.0 kPa), while the energy loss coefficient decreased from 68.6 to 46.9 (Fig. 4(e)). This enhanced cyclic stability originates from the three-dimensional cross-linked network structure formed during carbonization, where the structural integrity of the carbon

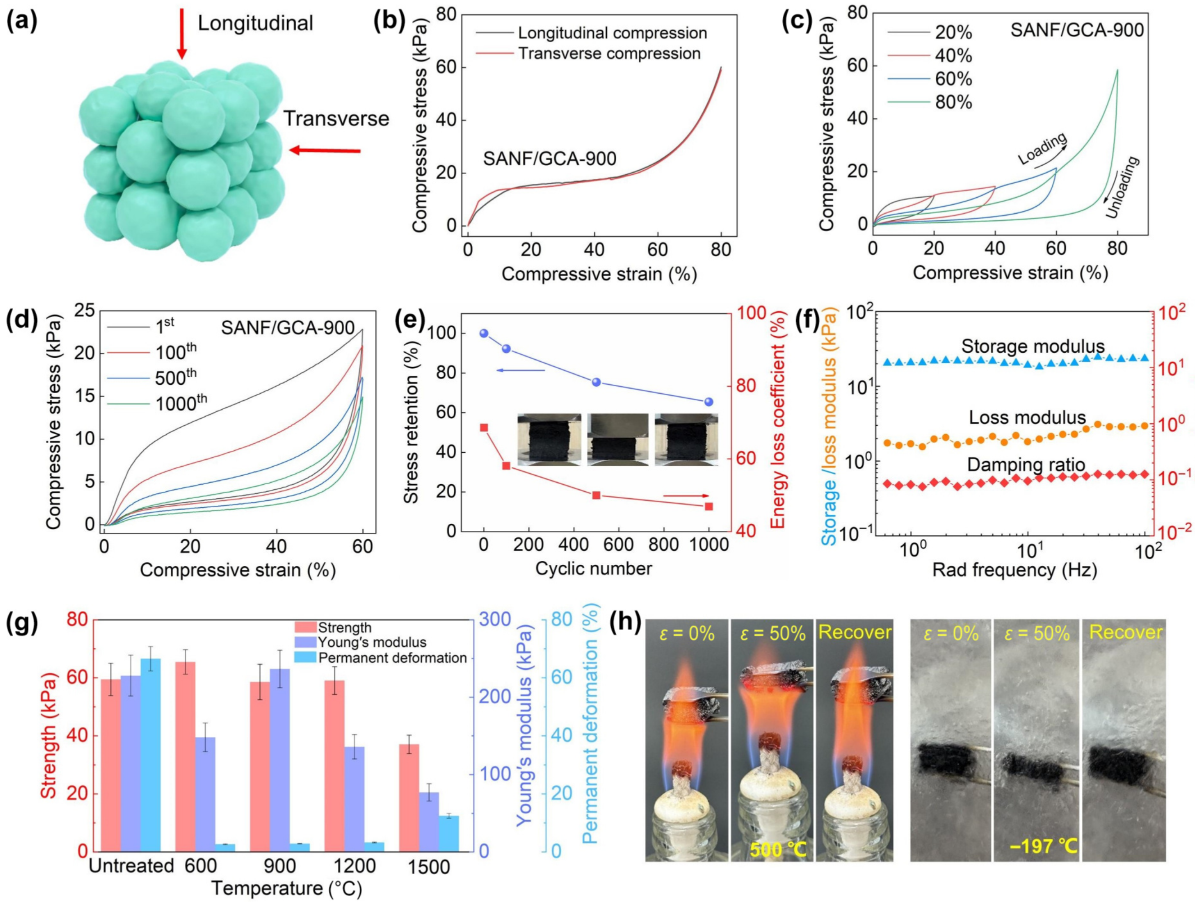

Figure 4 Mechanical performance of SANF/GCA. (a) Schematic illustration of SANF/GCA compressive deformation along transverse and longitudinal directions. (b) Compressive stress–strain profiles of the SANF/GCA-900 under uniaxial loading along both orientations, demonstrating directional isotropy at 80% strain. (c) Cyclic compression behavior of the SANF/GCA-900 showing loading-unloading curves at varying strain levels. (d) Long-term compression durability test at 60% strain, revealing structural integrity maintenance through 1000 compressive cycles. (e) Corresponding calculated stress retention and energy loss coefficient of the SANF/GCA-900 for different compressive cycles. (f) The dynamic viscoelastic response was characterized via frequency sweep tests using dynamic mechanical analysis. (g) Comparative analysis of compressive strength, Young's modulus, and permanent deformation parameters across thermally-treated composites: pristine SANF/GOA vs. SANF/GCA series (600, 900, 1200, and 1500 °C). (h) Optical images show the compressive resilience of ANFC aerogel under exposure to extreme environments of 500 and −197 °C.

skeleton effectively suppresses molecular chain slippage and structural creep. Comparative experiments further revealed the inhibitory effect of carbonization treatment on plastic deformation. Under 80% strain conditions, non-carbonized SANF/GOA exhibited substantial irreversible plastic deformation (Fig. S10 in the ESM), whereas carbonized SANF/GCA-900 demonstrated remarkable improvement, with plastic deformation consistently below 2.9% (Fig. 4(g)). This order-of-magnitude difference confirms that carbonization treatment significantly enhances elastic recovery performance by strengthening intermolecular interactions and constructing an energy dissipation network.

Dynamic mechanical analysis (DMA) elucidated the viscoelastic behavior of SANF/GCA-900 (Fig. 4(f)). The material displayed frequency-independent dynamic responses across 0.5–100 Hz: Storage modulus (G' = 21.4 kPa) and loss modulus (G'' = 2.2 kPa) exhibited minimal variation, with a consistent damping ratio of 0.1, suggesting energy dissipation primarily through elastic deformation rather than viscous flow. Wide-temperature compression tests (−197 to 500 °C) verified material reliability under thermal extremes (Fig. 4(h)). At 50% compressive strain, the material maintained structural stability without brittle fracture at cryogenic temperatures or interlayer collapse/plastic deformation at elevated temperatures. SEM images of the compressed sample under extreme conditions demonstrate that the three-dimensional spherical cavity structure exhibits no pore wall collapse or topological instability (Fig. S11 in the ESM), confirming the stability of its microstructure. This broad thermal adaptability originates from covalent bonding in the 3D carbon framework, ensuring dimensional stability during drastic temperature fluctuations.

2.5 Thermal insulation performance of SANF/GCA

As a representative porous insulating material, aerogel exhibits ultralow thermal conductivity owing to its unique 3D network structure [33, 35, 36]. In this study, the successfully fabricated SANF/GCA system achieves synergistic suppression of high porosity and gas–solid phase thermal conduction through microstructure regulation. Thermal imaging analysis (Fig. 5(a)) demonstrates that when the SANF/GCA-900 sample contacts a 100 °C heat source, its surface temperature rises merely to 38.7 °C within the initial 1 min and shows only a marginal increase to 40.8 °C after 10 min of continuous heating. The temperature evolution curves (Fig. 5(b)) further reveal that the material interface maintains a remarkable 53 °C temperature difference during steady-state heat transfer, conclusively verifying its exceptional thermal insulation performance.

Experimental results demonstrate that the SANF/GCA composite exhibits excellent thermal and electrical isotropy. The anisotropy index of both thermal conductivity and electrical conductivity in the radial and transverse directions is below 1.06 (Fig. 5(c) and Fig. S12 in the ESM), which primarily stems from its uniquely designed three-dimensional isotropic network structure. Notably, the overall thermal conductivity remains at a relatively low level (< 84.2 $\mathrm{mW \cdot m^{-1} \cdot K^{-1}}$), providing significant advantages for thermal management applications. Finite element-based numerical simulation illustrates the temperature distribution within a 2D random porous model subjected to a thermal gradient between 100 °C at the bottom and 35 °C at the top (Fig. 5(d)). Further analysis reveals that the heat flux is primarily concentrated in the interstitial regions between spherical cavities (Fig. S13 in the ESM).

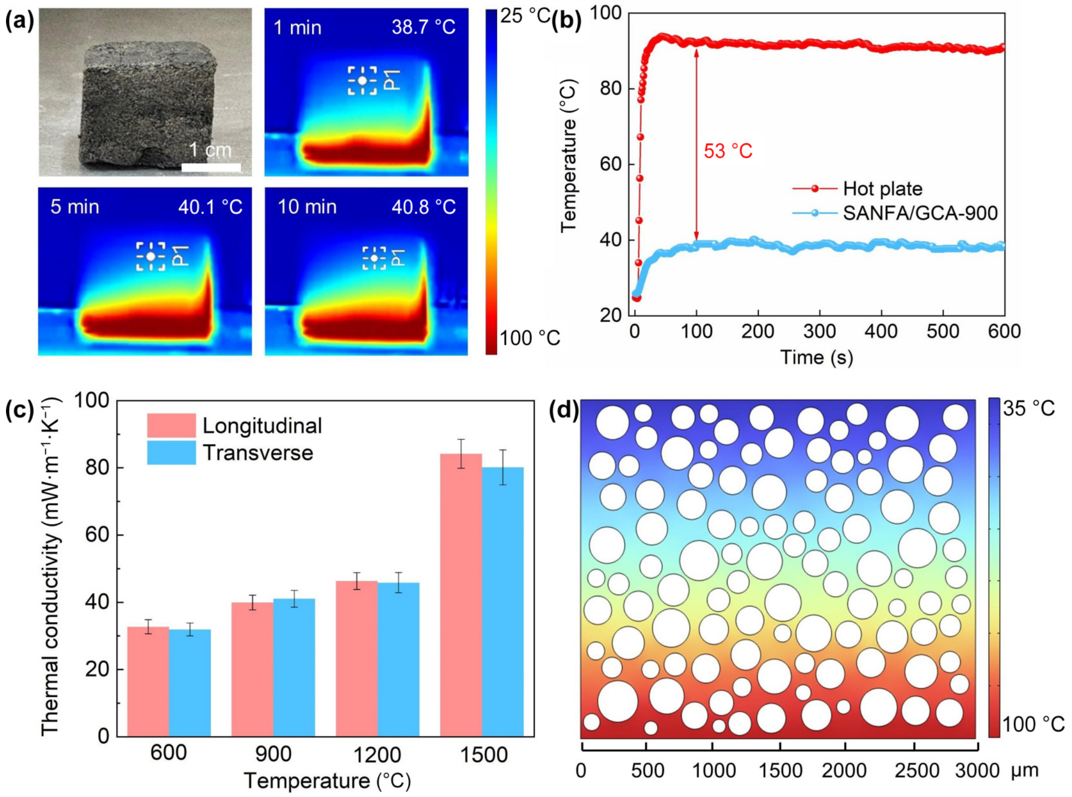

Figure 5 Thermal insulation performance of SANF/GCA. (a) Optical and infrared images of the SANF/GCA-900 heated at 100 °C. (b) Real-time temperature evolution profiles recorded during heating cycles of the SANF/GCA-900. (c) The thermal conductivity of SANF/GCA-600, SANF/GCA-900, SANF/GCA-1200, and SANF/GCA-1500. (d) The temperature distribution was examined through finite element simulations.

This distinctive thermal transport behavior originates from the slit structures serving as connecting nodes in the hierarchical porous network, forming heat flux convergence channels, which provide novel insights into thermal transport mechanisms in porous media. The combined thermophysical properties of low thermal conductivity and high stability endow SANF/GCA with significant application potential in cutting-edge fields such as spacecraft re-entry thermal protection systems and hypersonic vehicle insulation liners.

3 Conclusion

This study demonstrates the successful fabrication of three-dimensionally isotropic elastic carbon aerogels via a synergistic bubble-templating and freeze-casting approach. Incorporating GO as an interfacial regulator within ANF matrix substantially improves the kinetic stability of bubble templates during assembly. The resultant aerogel exhibits exceptional mechanical properties, maintaining ultralow plastic deformation (< 2.9%) even under 80% compressive strain while demonstrating remarkable elastic recovery. Thermal characterization reveals outstanding insulation performance, featuring an ultralow thermal conductivity (< 84.2 $mW\cdot m^{-1}\cdot K^{-1}$) and near-isotropic heat transfer behavior (anisotropy index < 1.06). The proposed design strategy opens new avenues for developing high-performance porous materials, showing significant application potential in extreme-condition thermal management systems.

4 Experimental section

4.1 Materials

Aramid fibers (Kevlar) were purchased from DuPont Co., Ltd. Graphene oxide was purchased from Cheng Yi Co., China. Dimethyl sulfoxide (DMSO, 99.7%), potassium hydroxide (KOH, 95%), and SDS were obtained from Shanghai Macklin Biochemical Technology Co., Ltd. All materials were used as received without further purification.

4.2 Preparation of SANF/GOA

ANF was synthesized from Kevlar fibers via a proton donor-assisted deprotonation method. Briefly, Kevlar fibers and an equivalent of KOH were dissolved in DMSO under continuous magnetic stirring at 70 °C for 96 h to obtain a homogeneous ANF/DMSO solution. The resulting solution was then diluted with deionized (DI) water and stirred for 30 min. The mixture was subsequently washed multiple times with ethanol and DI water to remove residual KOH and DMSO. The purified ANF were redispersed in DI water and mechanically stirred to form a stable aqueous dispersion with a concentration of 12.5 $mg\cdot mL^{-1}$. In parallel, a homogeneous GO dispersion (30 $mg\cdot mL^{-1}$) was prepared by high-pressure homogenization at 1500 bar for five cycles. The ANF and GO dispersions were uniformly mixed at varying ratios to prepare ANF/GO hybrid solutions with GO contents of 10 wt.%, 20 wt.%, and 30 wt.%, denoted as ANF/GO_{91}, ANF/GO_{82}, and ANF/GO_{73}, respectively. Subsequently, 10 wt.% SDS was added. The mixture was aerated at 2200 rpm for 30 s using a high-speed stirrer, generating a microbubble-rich solution. The resulting suspension was subsequently flash-frozen in liquid nitrogen (−196 °C) for 10 min. Finally, the frozen gel was subjected to freeze-drying at −55 °C under a vacuum of 22.8 Pa for 96 h to obtain the lightweight and porous SANF/GOA.

4.3 Preparation of SANF/GCA

Following freeze-drying, SANF/GOA were subjected to thermal annealing in a tube furnace under argon flow. A staged heating protocol was implemented: Samples were heated to target temperatures of 600, 900, 1200, and 1500 °C at a controlled ramp rate of 5 $°C\cdot min^{-1}$, with a 2-hour isothermal hold at each temperature to ensure structural stabilization.

4.4 Characterizations

SEM images were obtained using a field-emission JSM-7610F Plus microscope with an acceleration voltage of 5 kV. TEM images were captured using a HRTEM (JEM-2100F). The morphology of GO was collected by atomic force microscope (AFM), Asylum Research Cypher ES. XRD patterns were recorded on a Rigaku Smartlab using Cu Kα radiation (λ = 1.5406 Å) at a scanning rate of 3 $°\cdot min^{-1}$. FTIR spectra were acquired on a Nicolet 60-SXB IR instrument with attenuated total reflection (ATR) mode. Raman spectra were measured using a Horiba LabRAM HR Evolution system with a 532 nm excitation laser. Thermogravimetric (TG) analysis was conducted on a STA449F3 under a nitrogen atmosphere with a heating rate of 10 $°C\cdot min^{-1}$. Zeta potentials were obtained on Mastersizer 3000 (Malvern). Infrared images were captured using an infrared camera (ST9450). Thermal conductivity measurements were conducted by ASTM E1530 using a TPS2500S thermal analyzer (Hot Disk) employing the guarded heat flow meter technique. The electrical conductivity and sheet resistance were measured using a four-point probe system (RTS-9, Probes Technology) with a tunable constant current source (0.1–100 mA range). Optical microscopy images were acquired using an Olympus IX73 inverted fluorescence microscope. The viscosity of the samples was measured using an NDJ-8S rotational viscometer. Compressive tests were conducted on a universal testing machine (MTS E44.104, 4 $mm\cdot min^{-1}$).

Electronic Supplementary Material: Supplementary material (Figs. S1–S13) is available in the online version of this article at https://doi.org/10.26599/NR.2025.94907690.

Data availability

All data needed to support the conclusions in the paper are presented in the manuscript and the Electronic Supplementary Material. Additional data related to this paper may be requested from the corresponding author upon request.

Acknowledgement

The authors sincerely acknowledge financial support from the National Natural Science Foundation of China (No. 22279097), Natural Science Foundation of Hubei Province (No. 2025AFB038), and the Foundation of National Key Laboratory of Microwave Imaging Technology.

Declaration of competing interest

All the contributing authors report no conflict of interests in this work.

Author contribution statement

W. Q., Z. W., and D. P. H. designed the project. W. Q., H. Z. Z., L. L., X. L., and P. L. performed the preparation and processing of materials and data analysis. W. Q., H. Z. Z., L. L., and P. F. C. carried out the characterization and measurement. W. Q. and H. Z. Z. performed the simulation calculation. Z. W. and D. P. H. reviewed the manuscript. D. P. H. supervised the whole process. All authors participated in the discussion of the results, commented on the implications, and fully approved the content of the manuscript.

Use of AI statement

None.

References

[1] Lin, H.; Shen, Q. T.; Ma, M.; Ji, R. Q.; Guo, H. J.; Qi, H.; Xing, W.; Tang, H. P. 3D printing of porous ceramics for enhanced thermal insulation properties. *Adv. Sci.* **2025**, *12*, 2412554.

[2] Wu, L.; Li, Y.; Fu, Z. Y.; Su, B. L. Hierarchically structured porous materials: Synthesis strategies and applications in energy storage. *Natl. Sci. Rev.* **2020**, *7*, 1667–1701.

[3] Xiang, L. X.; Li, Q.; Li, C.; Yang, Q. Q.; Xu, F. G.; Mai, Y. Block copolymer self-assembly directed synthesis of porous materials with ordered bicontinuous structures and their potential applications. *Adv. Mater.* **2023**, *35*, 2207684.

[4] Yu, C.; Xie, B. L.; Yao, X. H.; Hu, N.; Guo, J. H.; Jiang, X. H.; Smith, A. T.; Sun, L. Y. Cabbage-like flexible fluororubber/carbon aerogel hybrids with negative Poisson's ratios and excellent microwave absorption. *Matter* **2023**, *6*, 4321–4338.

[5] Du, F. Y.; Jin, Z. Q.; Yang, R. Z.; Hao, M. L.; Wang, J. W.; Xu, G.; Zuo, W. Q.; Geng, Z. F.; Pan, H.; Li, T. et al. Thermally insulating and fire-retardant bio-mimic structural composites with a negative Poisson's ratio for battery protection. *Carbon Energy* **2023**, *5*, e353.

[6] Xu, X.; Zhang, Q. Q.; Hao, M. L.; Hu, Y.; Lin, Z. Y.; Peng, L. L.; Wang, T.; Ren, X. X.; Wang, C.; Zhao, Z. P. et al. Double-negative-index ceramic aerogels for thermal superinsulation. *Science* **2019**, *363*, 723–727.

[7] Yu, Z. L.; Qin, B.; Ma, Z. Y.; Huang, J.; Li, S. C.; Zhao, H. Y.; Li, H.; Zhu, Y. B.; Wu, H. A.; Yu, S. H. Superelastic hard carbon nanofiber aerogels. *Adv. Mater.* **2019**, *31*, 1900651.

[8] Su, L.; Wang, H. J.; Niu, M.; Fan, X. Y.; Ma, M. B.; Shi, Z. Q.; Guo, S. W. Ultralight, recoverable, and high-temperature-resistant SiC nanowire aerogel. *ACS Nano* **2018**, *12*, 3103–3111.

[9] Cheng, Y. F.; Xie, Y. M.; Liu, Z. Y.; Yan, S. W.; Ma, Y. N.; Yue, Y.; Wang, J. B.; Gao, Y. H.; Li, L. Y. Maximizing electron channels enabled by MXene aerogel for high-performance self-healable flexible electronic skin. *ACS Nano* **2023**, *17*, 1393–1402.

[10] Zhang, H. Y.; Wei, Z. C.; Wu, J. H.; Cheng, F.; Ma, Y. N.; Liu, W. J.; Cheng, Y. F.; Lin, Y. J.; Liu, N. S.; Gao, Y. H. et al. Interlayer-spacing-regulated MXene/rGO foam for multi-functional zinc-ion microcapacitors. *Energy Storage Mater.* **2022**, *50*, 444–453.

[11] Ji, X. D.; Zhao, X.; Zhang, Z. X.; Si, Y. F.; Qian, W.; Fu, H. Q.; Chen, Z. B.; Wang, Z.; Jin, H. H.; Yang, Z. G. et al. Scalable fabrication of graphene-assembled multifunctional electrode with efficient electrochemical detection of dopamine and glucose. *Nano Res.* **2023**, *16*, 6361–6368.

[12] Zhuang, L.; Lu, D.; Zhang, J. J.; Guo, P. F.; Su, L.; Qin, Y. B.; Zhang, P.; Xu, L.; Niu, M.; Peng, K. et al. Highly cross-linked carbon tube aerogels with enhanced elasticity and fatigue resistance. *Nat. Commun.* **2023**, *14*, 3178.

[13] Zhang, X. X.; Cheng, X. T.; Si, Y.; Yu, J. Y.; Ding, B. All-ceramic and elastic aerogels with nanofibrous-granular binary synergistic structure for thermal superinsulation. *ACS Nano* **2022**, *16*, 5487–5495.

[14] Zhang, P. P.; Li, J.; Lv, L. X.; Zhao, Y.; Qu, L. T. Vertically aligned graphene sheets membrane for highly efficient solar thermal generation of clean water. *ACS Nano* **2017**, *11*, 5087–5093.

[15] Zong, D. D.; Bai, W. Y.; Yin, X.; Yu, J. Y.; Zhang, S. C.; Ding, B. Gradient pore structured elastic ceramic nanofiber aerogels with cellulose nanonets for noise absorption. *Adv. Funct. Mater.* **2023**, *33*, 2301870.

[16] Zhao, H. Y.; Shu, C.; Wang, X.; Min, P.; Li, C. J.; Gao, F. L.; Li, X. F.; Yu, Z. Z. Bioinspired intelligent solar-responsive thermally conductive pyramidal phase change composites with radially oriented layered structures toward efficient solar-thermal-electric energy conversion. *Adv. Funct. Mater.* **2023**, *33*, 2302527.

[17] Hu, P. Y.; Wang, J.; Zhang, P. G.; Wu, F. S.; Cheng, Y. Y.; Wang, J.; Sun, Z. M. Hyperelastic Kevlar nanofiber aerogels as robust thermal switches for smart thermal management. *Adv. Mater.* **2023**, *35*, 2207638.

[18] Zhu, W. Q.; Zhuang, Y. H.; Weng, J. Q.; Huang, Q. Z.; Lai, G. B.; Li, L. Y.; Chen, M. X.; Xia, K. L.; Lu, Z. X.; Wu, M. M. et al. Evolution of naturally dried MXene-based composite aerogels with flash Joule annealing for large-scale production of highly sensitive customized sensors. *Adv. Mater.* **2024**, *36*, 2407138.

[19] Gao, H. L.; Wang, Z. Y.; Cui, C.; Bao, J. Z.; Zhu, Y. B.; Xia, J.; Wen, S. M.; Wu, H. A.; Yu, S. H. A highly compressible and stretchable carbon spring for smart vibration and magnetism sensors. *Adv. Mater.* **2021**, *33*, 2102724.

[20] Pan, F.; Shi, Y. Y.; Yang, Y.; Guo, H. T.; Li, L. X.; Jiang, H. J.; Wang, X.; Zeng, Z. H.; Lu, W. Porifera-inspired lightweight, thin, wrinkle-resistance, and multifunctional MXene foam. *Adv. Mater.* **2024**, *36*, 2311135.

[21] Cheng, P.; Liu, K.; Wan, Y. C.; Hu, W.; Ji, C. C.; Huang, P.; Guo, Q. H.; Xu, J.; Cheng, Q.; Wang, D. Solution viscosity-mediated structural control of nanofibrous sponge for RNA separation and purification. *Adv. Funct. Mater.* **2022**, *32*, 2112023.

[22] Gao, H. L.; Zhu, Y. B.; Mao, L. B.; Wang, F. C.; Luo, X. S.; Liu, Y. Y.; Lu, Y.; Pan, Z.; Ge, J.; Shen, W. et al. Super-elastic and fatigue resistant carbon material with lamellar multi-arch microstructure. *Nat. Commun.* **2016**, *7*, 12920.

[23] Yang, G. H.; Zhang, X. F.; Wang, R. J.; Liu, X.; Zhang, J. M.; Zong, L.; Yang, H. S. Ultra-stretchable graphene aerogels at ultralow temperatures. *Mater. Horiz.* **2023**, *10*, 1865–1874.

[24] Cheng, Y.; Zhang, X.; Qin, Y. X.; Dong, P.; Yao, W.; Matz, J.; Ajayan, P. M.; Shen, J. F.; Ye, M. X. Super-elasticity at 4 K of covalently crosslinked polyimide aerogels with negative Poisson's ratio. *Nat. Commun.* **2021**, *12*, 4092.

[25] Wu, J. P.; Wang, Y.; Zhang, J. S.; Zhao, C. Y.; Fan, Z. Y.; Shu, Q.; He, X. K.; Xuan, S. H.; Gong, X. L. A lightweight aramid-based structural composite with ultralow thermal conductivity and high-impact force dissipation. *Matter* **2022**, *5*, 2265–2284.

[26] Min, P.; Li, X. F.; Liu, P. F.; Liu, J.; Jia, X. Q.; Li, X. P.; Yu, Z. Z. Rational design of soft yet elastic lamellar graphene aerogels via bidirectional freezing for ultrasensitive pressure and bending sensors. *Adv. Funct. Mater.* **2021**, *31*, 2103703.

[27] Min, P.; Liu, J.; Li, X. F.; An, F.; Liu, P. F.; Shen, Y. X.; Koratkar, N.; Yu, Z. Z. Thermally conductive phase change composites featuring anisotropic graphene aerogels for real-time and fast-charging solar-thermal energy conversion. *Adv. Funct. Mater.* **2018**, *28*, 1805365.

[28] Yang, H. S.; Jin, X. T.; Sun, G. Q.; Li, Z. L.; Gao, J.; Lu, B.; Shao, C. X.; Zhang, X. Q.; Dai, C. L.; Zhang, Z. P. et al. Retarding Ostwald ripening to directly cast 3D porous graphene oxide bulks at open ambient conditions. *ACS Nano* **2020**, *14*, 6249–6257.

[29] Jin, J. K.; Wu, X. E.; Liang, H. R.; Wang, H. M.; Li, S.; Lu, H. J.; Bi, P.; Niu, J. L.; Wu, Y.; Zhang, Y. Y. A synergistic interfacial and topological strategy for reinforcing aramid nanofiber films. *Mater. Horiz.* **2023**, *10*, 4626–4634.

[30] Zong, D. D.; Bai, W. Y.; Geng, M.; Yin, X.; Yu, J. Y.; Zhang, S. C.; Ding, B. Bubble templated flexible ceramic nanofiber aerogels with cascaded resonant cavities for high-temperature noise absorption. *ACS Nano* **2022**, *16*, 13740–13749.

[31] Hu, P. Y.; Lyu, J.; Fu, C.; Gong, W. B.; Liao, J. H.; Lu, W. B.; Chen, Y. P.; Zhang, X. T. Multifunctional aramid nanofiber/carbon nanotube hybrid aerogel films. *ACS Nano* **2020**, *14*, 688–697.

[32] Wang, Z.; Mao, B. Y.; Zhao, M.; Calatayud, D. G.; Qian, W.; Li, P.; Hu, Z. G.; Fu, H. Q.; Zhao, X.; Yan, S. L. et al. Ultrafast macroscopic assembly of high-strength graphene oxide membranes by implanting an interlaminar superhydrophilic aisle. *ACS Nano* **2022**, *16*, 3934–3942.

[33] Qian, W.; Fu, H. Q.; Sun, Y.; Wang, Z.; Wu, H.; Kou, Z. K.; Li, B. W.; He, D. P.; Nan, C. W. Scalable assembly of high-quality graphene films via electrostatic-repulsion aligning. *Adv. Mater.* **2022**, *34*, 2206101.

[34] Ye, Z. M.; Fang, T.; Cong, C. N.; Chen, K.; Zhang, D.; Kong, X. B.; Wang, Q.; Liu, S. Z.; Li, M.; Zhao, B. et al. Strong and fatigue-resistant carbon nanotube composites enabled by amorphous/crystalline heterophase shell. *ACS Nano* **2024**, *18*, 24984–24996.

[35] Wang, G.; Feng, J. B.; Zhou, Z. Z.; Liu, Z.; Wu, J. P.; Li, J. C.; Gao, Q.; Lynch, M.; Li, J. Z.; Song, P. G. Low-cost hyperelastic fuller-dome-structured nanocellulose aerogels by dual templates for personal thermal management. *Adv. Mater.* **2025**, *37*, 2414896.

[36] Wang, Z. Y.; Li, Z. C.; Li, B.; Shi, A. F.; Zhang, L.; Zhu, Y. B.; Ye, F.; Yu, S. H. Functional carbon springs enabled dynamic tunable microwave absorption and thermal insulation. *Adv. Mater.* **2024**, *36*, 2412605.